Data-Driven Kalman Filter with Maximum Incremental Capacity Measurement for Battery State-of-Health Estimation

Onur Kadem, Jongrae Kim, *Senior member, IEEE*

***Abstract*—State of health (SoH) estimation is crucial for the reliable operation of battery management systems. While various SoH estimation approaches have been proposed, the integration of adaptive filtering with practical indirect health measurements remains insufficiently explored. This study introduces an online, data-driven SoH estimation framework that combines Gaussian process regression (GPR) with an extended Kalman filter (EKF). Moreover, the proposed method uses the normalized maximum incremental capacity measurement as a health indicator (HI). Extracting this HI during the constant current phase of the constant current constant voltage charging protocol enables online SoH estimation. The equivalent full cycle count is used for a priori prediction, while the HI is employed for a posteriori updates. Experimental validation of the method is carried out using three publicly available battery datasets, i.e., Dataset 1, Dataset 2, and Dataset 3, through a leave-one-battery-out cross-validation under varying operational conditions. The proposed GPR-EKF outperforms the EKF on Datasets 1-2 and is comparable on Dataset 3, while outperforming the Long Short-Term Memory-EKF across all datasets with average root mean square errors (RMSEs) of 1.88%, 0.45%, and 1.06%, respectively. Furthermore, the method exhibits robust SoH estimation, maintaining an RMSE of 0.91% even when the HI measurement is intermittently available with an 80% probability. These results highlight the potential of the proposed GPR-EKF method for accurate, robust, and online SoH estimation in practice.**

***Index Terms*—Lithium-ion Batteries; Battery Management System (BMS); State of Health (SoH) Estimation; Incremental Capacity Analysis (ICA); Extended Kalman Filter (EKF); Gaussian Process Regression (GPR); Online Monitoring**

I. Introduction

LITHIUM-ion batteries (LIBs) are widely used in consumer electronics and electric vehicles as a primary energy source. However, LIBs undergo capacity degradation over the long term. Battery state of health (SoH), defined as the ratio of the battery's current actual capacity to its initial capacity at the beginning of life [1], is used to assess this degradation. Calculating SoH remains challenging due to complex internal electrochemical reactions and varying operational conditions. To address these challenges and enhance calculation accuracy, various techniques have been developed, broadly categorized into model-based and data-driven methods [2].

Model-based methods relate SoH to variations in model parameters using empirical models, electrochemical models (EMs), or equivalent circuit models (ECMs). Singh et al. [3] proposed a semi-empirical model with parameters for temperature, discharge rate, and cycle count, enabling rapid and accurate SoH estimation from charge–discharge data. Cacciato et al. [4] used a second-order Thevenin ECM with an added resistor to model the capacity loss at high current rates and designed a physics-informed observer to estimate SoH from voltage comparison. Bartlett et al. [5] proposed a reduced-order EM with a dual nonlinear observer to estimate capacity loss only as cyclable lithium reduction. While EMs are computationally intensive, ECMs are simpler and better suited for onboard use with limited accuracy [6]. He et al. [7] combined a current-integral principle, second-order Thevenin ECM, and real-time open-circuit voltage characteristic to predict current and feed its error into a proportional–integral observer for SoH estimation. However, bias, drift, and noise in Hall-effect or shunt sensors can degrade the accuracy and stability of the method. In model-based methods, observer design is required, and SoH estimation accuracy is limited by the precision of model parameter identification [8].

Data-driven methods for SoH estimation rely on historical battery data to model degradation behaviour, without incorporating physical or electrochemical knowledge. Common approaches include Gaussian process regression (GPR) [9], random forest regression [10], and support vector regression [11], as well as deep learning models such as long short-term memory (LSTM) networks [12] and hybrid architectures combining LSTM with convolutional neural networks (NNs) [13]. While these methods typically need large datasets and high computing power, they offer high accuracy by using statistical and machine learning techniques [14]. To estimate SoH, Wang et al. introduced a physics-informed NN whose physical interpretability is constrained by empirical and state-space models [15]. Wu et al. [16] applied linear regression with recursive feature elimination, which is cost-efficient yet inadequate for capturing complex nonlinear SoH behavior. A crucial step in data-driven methods is the extraction of health indicators (HIs), which are SoH-related features that strongly correlate with battery degradation and provide insights into aging [17].

Various techniques for HI extraction have been employed in the SoH estimation of LIBs, which can be categorized into direct and indirect measurement methods. Internal resistance measurement via electrochemical impedance spectroscopy (EIS) is one of the most widely used direct measurement approaches [18]. EIS provides insights into battery impedance, which serves as a reliable proxy for SoH, as demonstrated by Kim et al. [19]. Coulomb counting is another direct measure-

(*Corresponding author: Onur Kadem.*)

Onur Kadem is with the Department of Mechanical Engineering, Bursa Technical University, Bursa, 16310, Türkiye (e-mail: onur.kadem@btu.edu.tr).

Jongrae Kim is with the School of Mechanical Engineering, University of Leeds, Leeds, LS2 9JT, United Kingdom (e-mail: menjkim@leeds.ac.uk).

ment method that estimates SoH by measuring ampere-hours during complete charge–discharge cycles [20]. Direct measurement methods offer accurate SoH assessment. However, EIS requires dedicated impedance-measurement hardware in a battery management system (BMS), and Coulomb counting requires at least one full charge/discharge cycle for a reliable SoH estimation. In contrast, indirect measurement methods address these limitations by relying on readily available operational data. For instance, Wang et al. [21] extracted charging data from the constant voltage (CV) charging phase, while Guo et al. [22] analyzed constant current (CC) phase data to derive a transformation function and time-based parameter to estimate SoH during the constant current–constant voltage (CCCV) charging process. Other indirect methods include incremental capacity analysis (ICA) [23], ultrasonic diagnostics for detecting internal structural anomalies [24], entropy-based approaches [25], differential thermal voltammetry [26], and wavelet packet energy entropy analysis [27]. These techniques enable non-destructive and efficient monitoring of battery health using measurable signals.

Among all the aforementioned HI extraction methods, ICA is widely used due to its ability to extract reliable aging characteristics from real-time operational data. Dubarru et al. [28] combined ICA and open circuit voltage for degradation source identification. Wang et al. [29] showed that changes in partial ICA curve areas reflect SoH loss. Stroe et al. [30] emphasised its strength in identifying capacity fade through ICA curve valleys. Wei et al. [31] applied ICA to estimate the SoH of lithium cobalt oxide (LCO) / lithium nickel cobalt oxide (NCO) batteries. The effectiveness of ICA for nickel manganese cobalt (NMC) batteries was demonstrated in [32]. Li et al. [33] extracted ICA peak features (height, position, and area) to train a support vector regression model, achieving a maximum absolute error below 2% in SoH prediction. Anseán et al. [34] showed that ICA curve peak height is a reliable SoH indicator for lithium iron phosphate (LFP) batteries, as it strongly correlates with lithium inventory loss.

Despite its potential, the integration of adaptive filtering techniques with indirect measurement approaches for battery SoH estimation remains underexplored, particularly in frameworks where the relationship between SoH and HIs is modelled using data-driven techniques. The availability of ICA during the CC phase of standard CCCV charging protocols enables its online implementation within a filtering framework. Utilising ICA-derived, physically interpretable, and low-dimensional features reduces the need for large training datasets and enables accurate and generalizable SoH estimation with limited data. To overcome the drawbacks of fully model-based and fully data-driven approaches while leveraging their respective advantages, this study introduces a hybrid SoH estimation framework that integrates ICA-derived features with an extended Kalman filter (EKF) informed by data-driven modelling. The proposed method offers a practical solution for real-time BMSs. The main contributions of this work are as follows:

1) Identification of a normalized ICA feature that reliably reflects battery health across diverse operational conditions.
2) Design procedure of an adaptive GPR-EKF framework that incorporates uncertainty from data-driven diagnostic features without requiring large-scale training datasets.
3) Experimental validation of the method using publicly available LIB datasets, including a case where HI measurements are not consistently available.

The structure of this paper is organised as follows: Section II outlines the methodology, including the extraction of health indicators and dataset description, the filter-based SoH estimation approach, followed by an explanation of the adaptive GPR-EKF method. Section III presents the experimental results, along with the hyperparameter settings and robustness tests. Finally, Section IV provides the conclusion and future research.

II. Methodology

To develop a filter-based SoH estimation algorithm, we first identify an HI, then establish polynomial prediction and measurement models. We design EKFs for SoH estimation using the polynomial models alone and with GPR and LSTM in separate variants.

A. Health indicator extraction

To identify accurate and robust HIs, choosing the CCCV charging mode is ideal as charging profiles are more stable and the SoH is not updated as frequently as the state of charge. This ensures that the extracted health features are consistent and reliable.

We explore the ICA method for assessing the HI of LIBs. ICA is a diagnostic technique used to assess the health and aging behavior of LIBs. It is based on the differentiation of the battery's charge capacity with respect to the terminal voltage of battery during the CC phase of a standard CCCV charging protocol. The ICA curve, represented as the incremental charge versus the terminal voltage, highlights characteristic peaks and valleys corresponding to electrochemical processes such as phase transitions and redox reactions within the electrode materials.

As the battery ages, these ICA curve features would undergo notable changes: peaks and valleys may shift in position, diminish in magnitude, or disappear entirely. These variations are associated with degradation mechanisms including the growth of the solid electrolyte interphase (SEI) layer, loss of active material, or increased internal resistance. Monitoring the evolution of these features over time enables early detection of degradation and supports accurate SoH estimation.

The incremental capacity (IC) is defined by

$$\mathrm{IC} = \frac{dQ}{dV} \tag{1}$$

where Q denotes the charge capacity in Coulomb and V is the terminal voltage in Volts. This formulation indicates that IC can be calculated from standard charge data, making it a practical tool for online health monitoring in BMSs. However, calculating derivatives from measured data can amplify noise, especially in high-resolution battery datasets, and the division could produce numerical overflows when the terminal voltage

TABLE I
DATASET 1, DATASET 2, AND DATASET 3 DETAILS

Parameter	Dataset 1	Dataset 2	Dataset 3
Battery type	Pouch	Pouch	Cylindrical
Cathode material	NMC	LCO/NCO	LFP
Nominal capacity	5000 mAh	740 mAh	1200 mAh
Charge voltage limit	4.2 V	4.2 V	3.6 V
Cut-off voltage	3.0 V	2.7 V	2 V
Charge current	0.5C	1C	2C
Discharge current	0.5C, 1.5C	1C	1.5C
Operating temperatures	0°C, 25°C, 45°C	40°C	No data
Batteries used	01, 03, 10, 11, 12	All (1-8)	51-55

remains close to a constant. To address this, the raw data must undergo preprocessing before differentiation. To mitigate high-frequency noise in the voltage–capacity data during ICA, a central difference approximation was applied when calculating the IC. Specifically, a symmetric window of size $2\omega + 1$ was used to compute the derivative as:

$$\frac{dQ}{dV} \approx \frac{\tilde{Q}(k+\omega) - \tilde{Q}(k-\omega)}{\tilde{V}(k+\omega) - \tilde{V}(k-\omega)} \tag{2}$$

where $\tilde{Q}$ and $\tilde{V}$ are the measured quantities that include sensor noise as follows:

$$\tilde{Q}(k \pm \omega) = Q(k \pm \omega) + n_q(k \pm \omega) \tag{3a}$$

$$\tilde{V}(k \pm \omega) = V(k \pm \omega) + n_v(k \pm \omega) \tag{3b}$$

where n_q and n_v are zero-mean Gaussian white noise whose ranges are typically around ± 10 mAs and ± 1 mV, respectively [35]. Substitute (3) into (2)

$$\frac{dQ}{dV} \approx \frac{\Delta Q + \Delta n_q}{\Delta V + \Delta n_v} = \frac{\Delta Q/\Delta V + \Delta n_q/\Delta V}{1 + \Delta n_v/\Delta V} \approx \frac{\Delta Q}{\Delta V} \tag{4}$$

where $\Delta(\cdot)$ is the difference of the quantity corresponding to $(\cdot)$, ω is chosen such that ΔV is big enough compared to Δn_q and Δn_v and at the same time ω is small enough to approximate the derivative by the finite difference. It is found that ω equal to 5 s is appropriate for the approximation during the CC phase of CCCV charging process. This calculation method can be replaced by more advanced numerical differentiators [36].

This research utilizes three open-source datasets, referred to as Dataset 1, Dataset 2 and Dataset 3. Table I summarizes the datasets. Dataset 1 [37] consists of 21 NMC111-based pouch batteries. Each battery was subjected to distinct aging protocols involving variations in charge/discharge C-rates, depth-of-discharge (DoD), cycling profiles, and operating temperatures. For the purposes of ICA, three specific criteria were considered essential: i) the lowest available constant-current charge rate to ensure sufficient resolution of electrochemical features, ii) full 100% DoD cycling to capture all distinguishable electrochemical features across the full voltage range, and iii) progression of aging down to at least approximately 80% SoH to allow meaningful degradation analysis. Based on these criteria, five batteries (01, 03, 10, 11, and 12) were selected. All were charged at 0.5C to ensure consistent ICA curve comparison. Aging temperatures were 25°C for Batteries 01 and 10, 45°C for Batteries 03 and 12, and 0°C for Battery 11. Discharge rates were 0.5C for Batteries 01 and 03, and 1.5C for Batteries 10, 11, and 12.

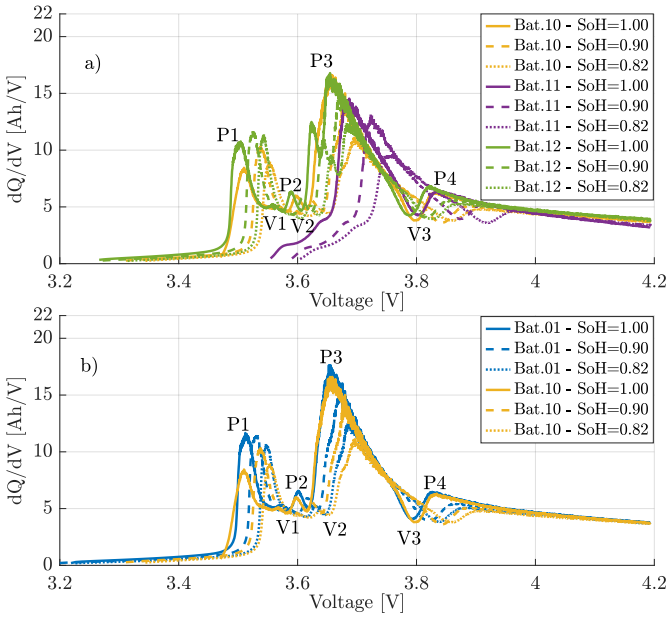

Fig. 1. (Dataset 1) Comparison of IC curves under different aging conditions: a) Effect of temperature: battery 10 (1.5C, 25°C), battery 11 (1.5C, 0°C), and battery 12 (1.5C, 45°C); b) Effect of discharge rate: battery 01 (0.5C, 25°C) vs. battery 10 (1.5C, 25°C).

Dataset 2 [38] consists of eight pouch batteries with LCO/NCO cathode chemistry. These batteries were tested in a controlled environment at a constant temperature of 40°C using a thermal chamber. Characterization measurements were conducted at intervals of every 100 cycles to monitor battery performance over time. These measurements were carried out by charging and discharging the battery at 1C. However, some batteries exhibited capacity dips during testing. Despite this, all batteries were retained for model development, as they provide diverse degradation behaviors that contribute to a more comprehensive understanding of the battery performance.

Dataset 3 [39] includes battery aging data from 64 LFP cylindrical batteries. Batteries underwent aging through CCCV cycling, with a reference performance test conducted approximately every 100 cycles. Five batteries (51-55) were selected because only these batteries were tested for a full 100% DoD. The batteries were charged at 2C and discharged at 1.5C.

For all datasets, the current battery capacity is calculated using the Coulomb counting method by integrating the load current over time during complete charge–discharge cycles. By definition, the SoH is expressed as [1]:

$$\text{SoH} = \frac{\int I(t)dt}{Q_{\text{rated}}} \tag{5}$$

where $I(t)$ is the load current as a function of time, and Q_{rated} is the nominal capacity at the beginning of life.

Fig. 1a) and 1b) present ICA curves at various SoH levels, measured under differing temperature conditions and cycling discharge rates, respectively. At 25°C and 45°C, four distinct peaks (P1, P2, P3, and P4) and three valleys (V1, V2, and V3) are apparent. In contrast, at 0°C, the absence of peaks P1 and P2 and valleys V1 and V2 reflects the suppression of electrochemical activity at low temperatures. Progressive

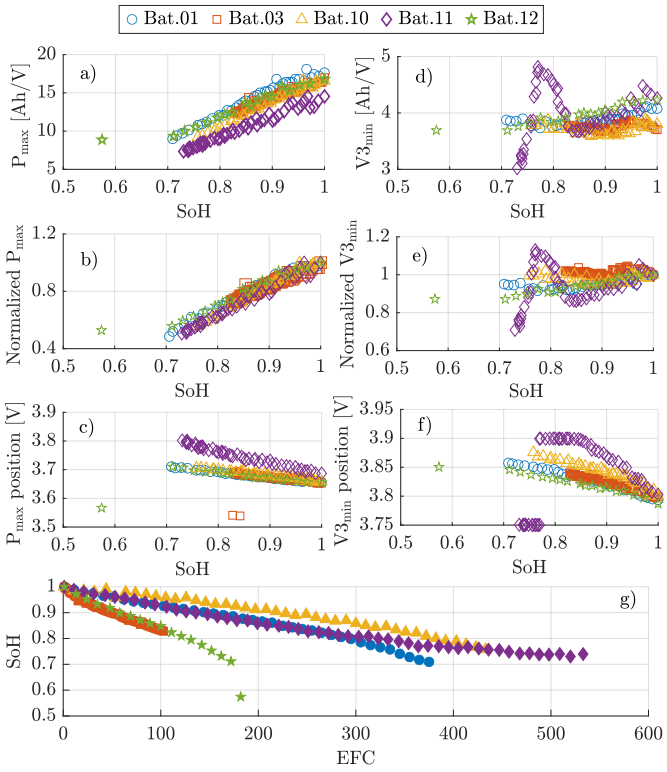

Fig. 2. (Dataset 1) Extracted IC features under different aging conditions: a) P3 peak magnitude; b) normalized P3 magnitude; c) P3 voltage position; d) V3 valley magnitude; e) normalized V3 magnitude; f) V3 voltage position; and g) cycle number versus SoH.

battery aging leads to a reduction in the amplitude of peak P4, increasing the significance of peak P3 and valley V3 for subsequent analysis. The magnitude of the most prominent peak, denoted as P_{max}, and its position remain relatively stable between 25°C and 45°C at comparable SoH levels. However, at 0°C, P3 not only decreases in magnitude but also shifts toward the higher voltage plateau, indicating kinetic constraints under these conditions. Furthermore, variations in discharge rate at 25°C influence both P_{max} and the location of P3; higher discharge rates accelerate capacity degradation, resulting in a lower P_{max} and a positional shift of P3 toward higher voltages. The characteristics of valley V3 also correlate with battery aging. Specifically, as the battery degrades, the magnitude of V3 diminishes modestly, and its position migrates toward higher voltages, though without a strictly monotonic pattern. The sensitivity of P3 and V3 to aging underscores their utility as an HI.

Fig. 2 illustrates the evolution of peak P3 and valley V3 as batteries age, along with the SoH as a function of equivalent full cycle (EFC) for multiple batteries subjected to various cycling conditions. Across all batteries, P_{max} demonstrates a consistent trend but differs in absolute value depending on the operational conditions, Fig. 2a). Therefore, the normalized P_{max}, calculated dividing by its value at SoH equal to 1, is incorporated as a candidate HI, Fig. 2b). The position of P3, Fig. 2c), exhibits a systematic shift toward higher voltage plateau as aging progresses, reflecting increased internal resistance and kinetic limitations; however, the rate of this

TABLE II
PEARSON r_p VALUES BETWEEN SOH AND SELECTED FEATURES.

Feature	P_{max} [Ah/V]	Normalized P_{max}	P_{max} position [V]
r_p	0.8356	0.9842	0.8013
Feature	$V3_{min}$ [Ah/V]	Normalized $V3_{min}$	$V3_{min}$ position [V]
r_p	0.6903	0.7217	0.5641

shift varies between batteries, corresponding to differences in degradation rates.

Both the V3 magnitude, Fig. 2d), and its normalized form, Fig. 2e), display greater nonlinearity and sensitivity under different temperature conditions, suggesting these features are more affected by environmental factors than those related to P3. The position of V3 remains relatively stable near 3.9 V for SoH between approximately 0.85 and 0.78, before dropping sharply to 3.75 V, Fig. 2f). This abrupt transition introduces a discontinuity that limits the utility of V3 position as an HI over the full lifetime at low temperatures. Finally, Fig. 2g) displays the SoH degradation trajectories, highlighting the accelerated capacity fade at elevated temperatures. Batteries 03 and 12 reach 80% SoH in less than 130 cycles, while Batteries 01 and 11 require approximately 300 cycles to reach the same threshold. In comparison, Battery 10 reaches 80% SoH after approximately 400 cycles.

To quantitatively analyze the correlation between the selected features and SoH, we performed a Pearson correlation analysis whose formula [40] is given by

$$r_p = \frac{\sum_{i=1}^{N}(x_i - \bar{x})(y_i - \bar{y})}{\sqrt{\sum_{i=1}^{N}(x_i - \bar{x})^2}\sqrt{\sum_{i=1}^{N}(y_i - \bar{y})^2}} \tag{6}$$

where r_p is the Pearson correlation coefficient, x_i refers to the information of each peak or valley, y_i denotes the SoH, $\bar{(\cdot)}$ is the mean of $(\cdot)$. The Pearson correlation coefficient is commonly interpreted within five categories between 0 and 1, with intervals of 0.2 corresponding to extremely low, low, moderate, strong, and extremely strong levels of association. Table II summarizes the r_p values and shows that normalization increases the P_{max}–SoH correlation coefficient from 0.8356 to 0.9842, moving it from the strong category to the extremely strong category.

For Dataset 2, a distinct dominant peak is observed for each charging cycle for each battery as shown in Fig. 3. During early cycles, smaller secondary peaks appear near 3.6 V, but they consistently remain lower than the main peak. With increasing EFC, P_{max} gradually diminishes. This decline indicates the loss of active lithium inventory and structural degradation in the electrode materials. As the battery ages, electrochemical activity decreases, reducing its ability to intercalate lithium ions, reflected by a lower P_{max} in the IC curve.

The relationship between the normalized P_{max} and SoH exhibits a consistent trend across all batteries, as illustrated in Fig. 4a). Furthermore, among the eight batteries, Batteries 4 to 6 underwent half the number of EFCs compared to the remaining batteries as shown in Fig. 4b). This observation

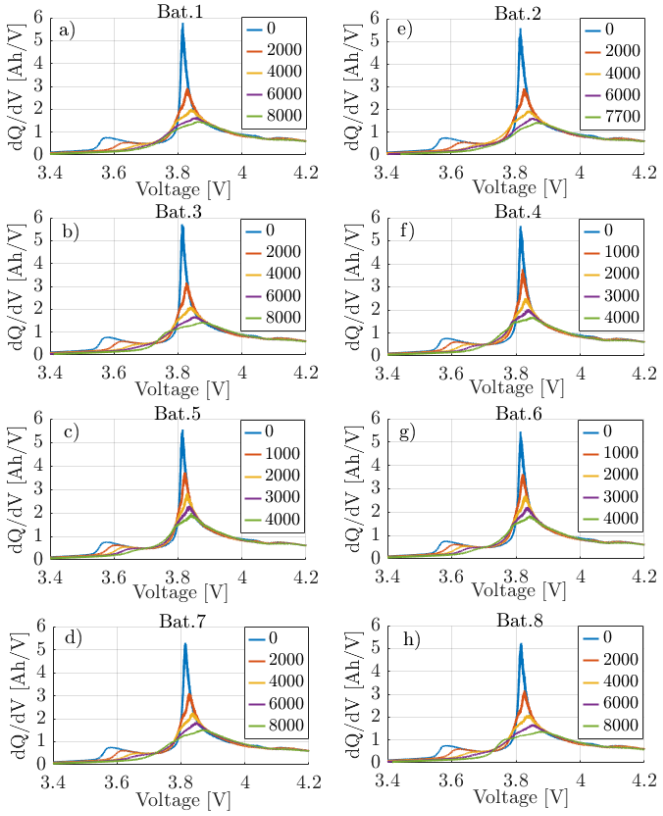

Fig. 3. (Dataset 2) Variation in IC curves with increasing EFC count between 0 and 4,000 or up to 8,000

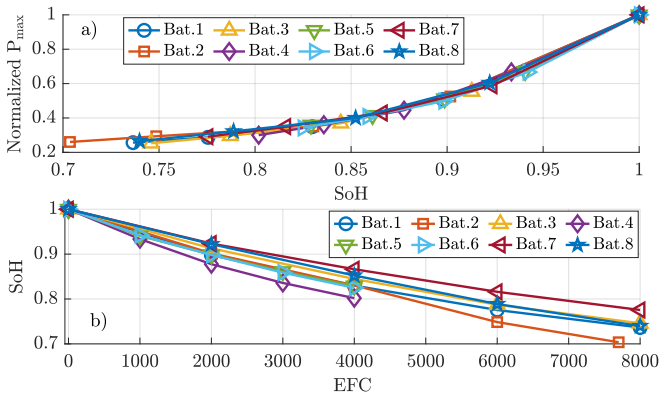

Fig. 4. (Dataset 2) Extracted IC feature and SoH trend with EFC: a)Normalized IC peak magnitudes as a function of SoH, b) SoH degradation trend as a function of EFC

suggests that normalized P_{max} is primarily a function of SoH rather than EFCs, highlighting its effectiveness as a reliable HI of battery SoH.

For Dataset 3, Fig. 5 illustrates a single primary dominant peak at each cycling step for every battery, similarly to Dataset 2. Figs. 6a) and 6b) demonstrate that the SoH-Normalized P_{max} and EFC–SoH relationships exhibit consistent and systematic trends, respectively.

Overall, normalized P_{max} emerges as the most robust and consistent feature under different operational conditions, maintaining a nearly constant relationship with SoH across all

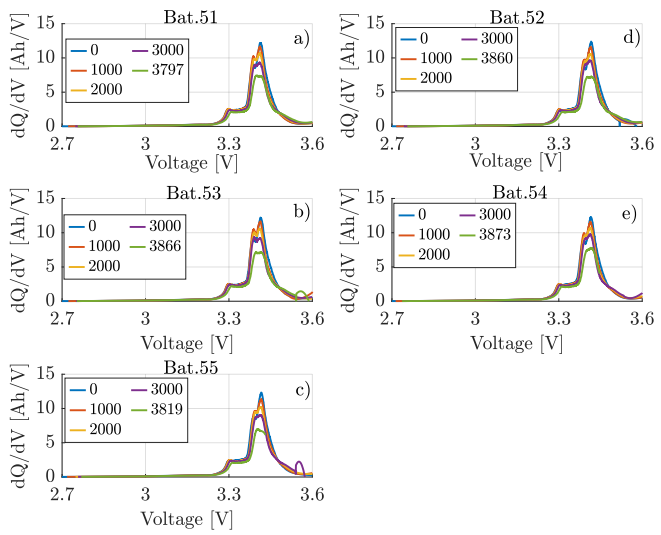

Fig. 5. (Dataset 3) Variations in IC curves with increasing EFC count between 0 and 3873

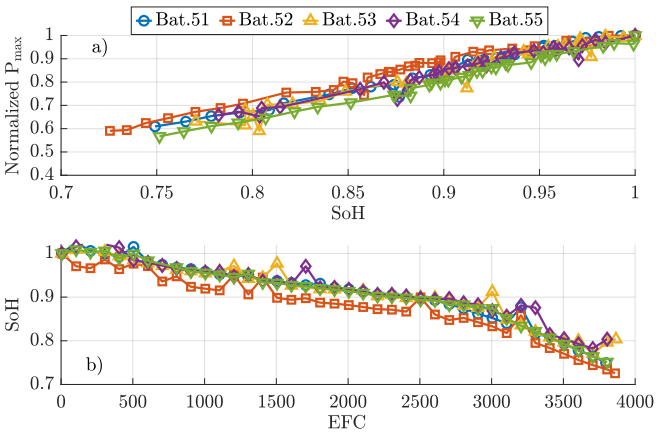

Fig. 6. (Dataset 3) Extracted IC feature and SoH trend with EFC: a)Normalized IC peak magnitudes as a function of SoH, b) SoH degradation trend as a function of EFC

batteries. This stability and insensitivity to varying operational conditions highlight its suitability for online SoH estimation, particularly under CCCV charging protocols, thereby reinforcing its practical relevance for real-world battery health assessment.

B. Polynomial Model & Filter-Based SoH Estimation

Figs. 7, 8 and 9 illustrate the performance of polynomial curve fitting for a given SoH providing the normalized P_{max} and for a given EFC count providing SoH across varying polynomial degrees for Datasets 1, 2 and 3, respectively. For the EFC-SoH relations, increasing the polynomial degree from 2 to 3 yields negligible improvement in root mean square error (RMSE)—remaining unchanged for Dataset 2 and showing only a minor reduction for Datasets 1 and 3. Therefore, a second-order polynomial is selected for the EFC-SoH. In contrast, the SoH-Normalized P_{max} achieves the highest performance with a third-order polynomial, yielding an RMSE of 0.0140 and R^2 of 0.9951 for Dataset 2, an RMSE

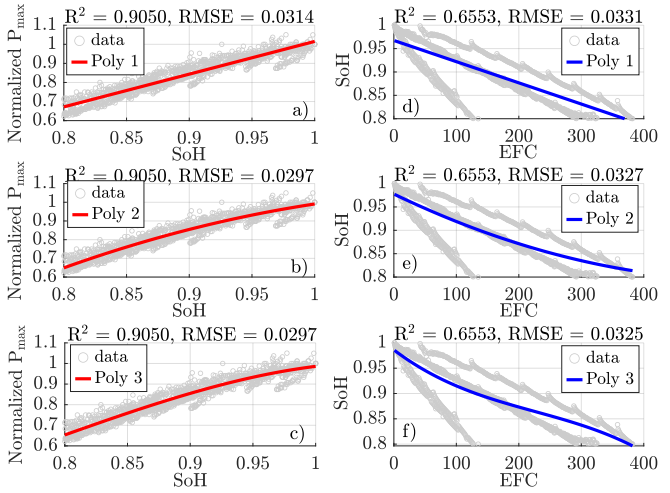

Fig. 7. (Dataset 1) Polynomial fitting for Dataset 1. Each subplot shows data from all batteries. Red lines in a), b), and c) and blue lines in d), e), and f) indicate polynomial fits. Poly $(\cdot)$ refers to $(\cdot)$-th order polynomial.

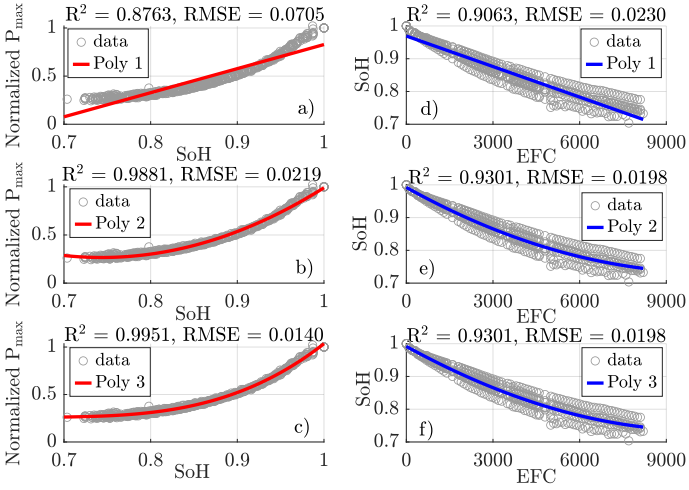

Fig. 8. (Dataset 2) Polynomial fitting for Dataset 2. Each subplot shows data from all batteries. Red lines in a), b), and c) and blue lines in d), e), and f) indicate polynomial fits. Poly $(\cdot)$ refers to $(\cdot)$-th order polynomial.

of 0.0172 and R^2 of 0.9780 for Dataset 3. The model yielded an RMSE of 0.0297 and R^2 of 0.9050 for Dataset 1. Thus, a third-order polynomial is employed for SoH-Normalized P_{max} relations.

Results from three datasets reveal that the SoH does not degrade equally with EFC count, as illustrated in Fig. 2g), Fig. 4b) and Fig. 6b). Despite this variability, the underlying EFC–SoH relationship provides useful prior knowledge for SoH estimation. To compensate the variability in the SoH estimation, we use a recursive SoH tracking using the EKF. To design the EKF, we propose a predictive model and a measurement model.

The observed SoH degradation trend as a function of EFC is approximated using a second-order polynomial model as follows:

$$\mathrm{SoH}(u) = a_1 u^2 + a_2 u + a_3 \tag{7}$$

where u denotes the EFC count, and a_1, a_2 and a_3 are model

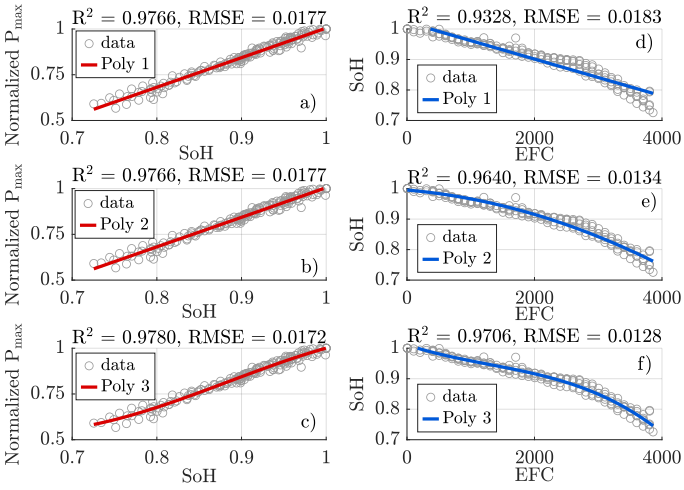

Fig. 9. (Dataset 3) Polynomial fitting for Dataset 3. Each subplot shows data from all batteries. Red lines in a), b), and c) and blue lines in d), e), and f) indicate polynomial fits. Poly $(\cdot)$ refers to $(\cdot)$-th order polynomial.

coefficients. Since SoH is normalized such that SoH $= 1$ at $u = 0$, it follows directly that $a_3 = 1$. The EFC count for partial cycling is computed as:

$$u = \frac{\sum_{i=1}^{N} \int_{t_{i,\mathrm{start}}}^{t_{i,\mathrm{end}}} I(t)\, dt}{Q_{\mathrm{rated}}} \tag{8}$$

where N denotes the total number of discharge events, $I(t)$ is the discharge current, and $t_{i,\mathrm{start}}$ and $t_{i,\mathrm{end}}$ represent the start and end times of the i-th discharge interval, respectively.

To facilitate recursive estimation, we define the next step EFC, u_{k+1}, using the current step EFC, u_k, and the current increment, Δu_k, as follows: $u_{k+1} = u_k + \Delta u_k$, where the step $k+1$ is the next full or partial completion of the CCCV charging process and k is the current full or partial completed CCCV charging process. Substituting this into Eq. (7) with the process noise yields the following recursive formulation as a prediction model for the EKF:

$$\begin{aligned}
\mathrm{SoH}_{k+1} &= a_1(u_k + \Delta u_k)^2 + a_2(u_k + \Delta u_k) + a_3 + w_k \\
&= a_1\left(u_k^2 + 2u_k\Delta u_k + \Delta u_k^2\right) \\
&\qquad + a_2 u_k + a_2\Delta u_k + a_3 + w_k \\
&= a_1 u_k^2 + a_2 u_k + a_3 + 2a_1 u_k \Delta u_k \\
&\qquad + a_1\Delta u_k^2 + a_2\Delta u_k + w_k \\
&= \mathrm{SoH}_k + 2a_1 u_k\Delta u_k + a_1\Delta u_k^2 + a_2\Delta u_k + w_k
\end{aligned} \tag{9}$$

where SoH_{k+1} and SoH_k are $\mathrm{SoH}(u_{k+1})$ and $\mathrm{SoH}(u_k)$, respectively, and $w_k \sim \mathcal{N}(0, q)$ denotes the zero-mean Gaussian process noise with the variance equal to q. The unmodeled or hidden dynamics is represented by the process noise.

The normalized P_{max}, measured during CC phase of CCCV charging, i.e., $\tilde{P}_{\mathrm{max},k}$, provides the following measurement model for the EKF:

$$\tilde{P}_{\mathrm{max},k} = b_1\mathrm{SoH}_k^3 + b_2\mathrm{SoH}_k^2 + b_3\mathrm{SoH}_k + b_4 + v_k \tag{10}$$

TABLE III
POLYNOMIAL, GPR, AND LSTM MODEL PERFORMANCES ON DATASETS 1, 2, AND 3

Dataset	Battery	Poly Pred. Model R^2 / RMSE	Poly Meas. Model R^2 / RMSE	GPR Pred. Model R^2 / RMSE	GPR Meas. Model R^2 / RMSE	LSTM Pred. Model R^2 / RMSE	LSTM Meas. Model R^2 / RMSE
Dataset 1	Bat.01	0.9509 / 0.0217	0.9725 / 0.0361	0.9173 / 0.0220	0.9730 / 0.0360	0.8106 / 0.0347	0.9409 / 0.0347
	Bat.03	0.9903 / 0.0612	0.9525 / 0.0192	0.9757 / 0.0581	0.9503 / 0.0198	0.8972 / 0.0630	0.9376 / 0.0173
	Bat.10	0.9347 / 0.0618	0.9785 / 0.0254	0.7881 / 0.0494	0.9772 / 0.0256	0.8036 / 0.0575	0.9545 / 0.0285
	Bat.11	0.9594 / 0.0266	0.9173 / 0.0430	0.8880 / 0.0277	0.9174 / 0.0432	0.8703 / 0.0285	0.9029 / 0.0451
	Bat.12	0.9951 / 0.0649	0.9538 / 0.0442	0.9541 / 0.0627	0.9508 / 0.0444	0.8334 / 0.0984	0.8869 / 0.0468
	Avg.	0.9661 / 0.0472	0.9549 / 0.0336	0.9046 / 0.0440	0.9537 / 0.0338	0.8430 / 0.0564	0.9246 / 0.0345
Dataset 2	Bat.1	0.9910 / 0.0072	0.9944 / 0.0146	0.9901 / 0.0076	0.9950 / 0.0138	0.9876 / 0.0084	0.9946 / 0.0142
	Bat.2	0.8962 / 0.0282	0.9951 / 0.0138	0.8963 / 0.0282	0.9933 / 0.0162	0.8938 / 0.0285	0.9931 / 0.0163
	Bat.3	0.9853 / 0.0090	0.9954 / 0.0138	0.9852 / 0.0090	0.9968 / 0.0115	0.9625 / 0.0144	0.9920 / 0.0182
	Bat.4	0.8150 / 0.0288	0.9962 / 0.0128	0.8109 / 0.0291	0.9962 / 0.0129	0.8341 / 0.0272	0.9956 / 0.0137
	Bat.5	0.7966 / 0.0311	0.9938 / 0.0153	0.7969 / 0.0311	0.9969 / 0.0109	0.8048 / 0.0304	0.9949 / 0.0138
	Bat.6	0.9755 / 0.0093	0.9922 / 0.0175	0.9741 / 0.0096	0.9942 / 0.0150	0.9715 / 0.0100	0.9875 / 0.0220
	Bat.7	0.7119 / 0.0341	0.9925 / 0.0165	0.7119 / 0.0341	0.9939 / 0.0148	0.6122 / 0.0395	0.9898 / 0.0192
	Bat.8	0.9579 / 0.0153	0.9942 / 0.0148	0.9581 / 0.0153	0.9954 / 0.0133	0.9066 / 0.0228	0.9949 / 0.0137
	Avg.	0.8912 / 0.0204	0.9942 / 0.0149	0.8904 / 0.0205	0.9952 / 0.0136	0.8716 / 0.0227	0.9928 / 0.0164
Dataset 3	Bat.51	0.9770 / 0.0109	0.9943 / 0.0090	0.9937 / 0.0057	0.9951 / 0.0084	0.9332 / 0.0186	0.9406 / 0.0290
	Bat.52	0.9875 / 0.0087	0.9914 / 0.0108	0.9967 / 0.0045	0.9943 / 0.0088	0.8918 / 0.0257	0.9286 / 0.0310
	Bat.53	0.9724 / 0.0107	0.9836 / 0.0145	0.9917 / 0.0059	0.9833 / 0.0146	0.8808 / 0.0222	0.9561 / 0.0237
	Bat.54	0.9693 / 0.0108	0.9817 / 0.0137	0.9877 / 0.0069	0.9816 / 0.0138	0.8006 / 0.0276	0.9332 / 0.0262
	Bat.55	0.9923 / 0.0064	0.9924 / 0.0105	0.9958 / 0.0047	0.9934 / 0.0098	0.9577 / 0.0149	0.9407 / 0.0294
	Avg.	0.9797 / 0.0095	0.9887 / 0.0117	0.9931 / 0.0055	0.9895 / 0.0111	0.8928 / 0.0218	0.9398 / 0.0279

where b_1, b_2, b_3 and b_4 are regression coefficients. $v_k \sim \mathcal{N}(0, r)$ denotes the zero-mean Gaussian measurement noise with the variance equal to r. Note that if the CCCV charge does not encompass the voltage region between 3.6–3.85 V for Dataset 1, 3.8–3.9 V for Dataset 2, or 3.35–3.50 V for Dataset 3, $\tilde{\mathrm{P}}_{\max,k}$ may not be available.

Eqs. (9) and (10) together define a state-space model as follows:

$$\begin{aligned} x_{k+1} &= Ax_k + BU_k + w_k \\ z_k &= h(x_k) + v_k \end{aligned} \tag{11}$$

where $x_k = \mathrm{SoH}_k$, $z_k = \tilde{\mathrm{P}}_{\max,k}$, $U_k = [u_k \Delta u_k,\ \Delta u_k^2,\ \Delta u_k]^T$, $A = 1$, $B = [2a_1, a_1, a_2]$, and $h(x_k) = b_1 x_k^3 + b_2 x_k^2 + b_3 x_k + b_4$. This is one of the standard forms for the EKF design, where the prediction model is linear and the measurement model is nonlinear.

While the polynomial models provide a reasonable approximation of the average SoH trajectory, they are limited in capturing battery-to-battery variability and nonlinear degradation patterns. To address these limitations and improve the performance of the EKF, a more flexible probabilistic model is introduced next.

C. GPR Model Based Extended Kalman Filter

GPR is a non-parametric Bayesian approach that captures nonlinear relationships and quantifies prediction uncertainty, making it well-suited for individualized battery health modeling. GPR defines a distribution over functions, offering both a predictive mean and a variance at each input. From Eq. (9), the training data set for the prediction model is defined as $\mathcal{D}_p = \{(i_k, o_k)\}_{k=1}^n$, where the input vector is $i_k = [\mathrm{SoH}_k, u_k, \Delta u_k]^T$ and the output vector is $o_k = [\mu_k, \sigma_k]^T$, where μ_k denotes the SoH mean prediction at the k-th charge cycle, and σ_k represents the associated predictive uncertainty. The relationship between inputs and outputs is modeled as

$$o_k = f(i_k) + \epsilon_k, \quad \epsilon_k \sim \mathcal{N}(0, \sigma_n^2) \tag{12}$$

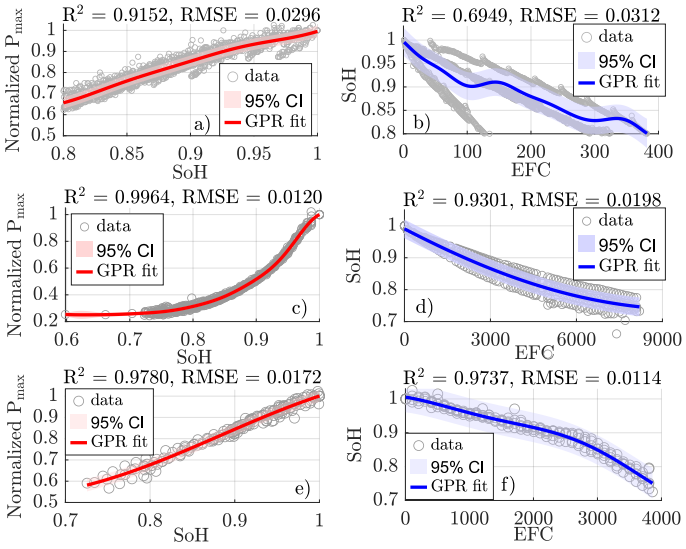

Fig. 10. GPR fitting for data from all batteries. Red and blue lines indicate measurement and prediction fits, respectively. a) and b) show results for Dataset 1, c) and d) for Dataset 2, e) and f) for Dataset 3.

where $f(\cdot)$ follows a Gaussian process prior, i.e., $f(\cdot) \sim \mathcal{GP}(\mu(i), k(i, i'))$, with mean function $\mu(\cdot)$ and kernel function $k(\cdot, \cdot)$ and ϵ_k is the measurement noise [42].

GPR model is employed to model the prediction and measurement models. Fig. 10 b), d) and f) present the GPR-based prediction and a), c) and e) present measurement models for Datasets 1, 2, and 3, respectively. For the measurement model, GPR achieves superior performance over the third-order polynomial model on Dataset 2, yielding an RMSE of 0.0120 and an R^2 of 0.9964. The GPR and third-order polynomial models have similar performances in Datasets 1 and 3. For the prediction model, GPR exhibits an advantage on Dataset 1, yielding an RMSE of 0.0312 and outperforming the second-

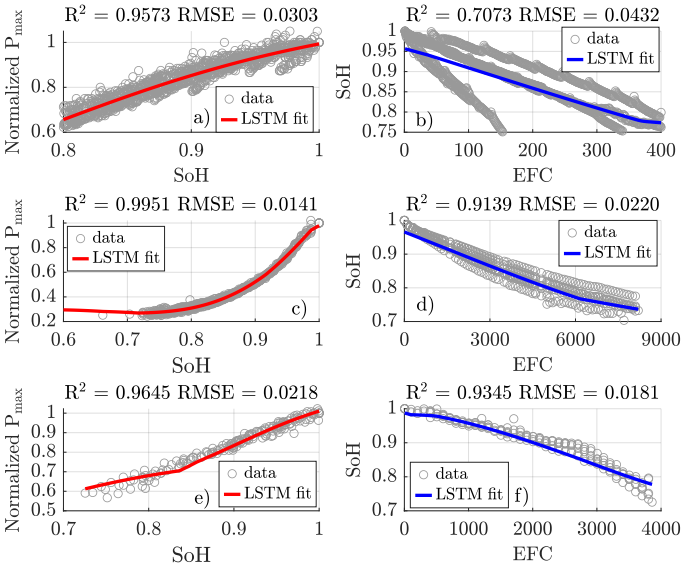

Fig. 11. LSTM fitting for data from all batteries. Red and blue lines indicate measurement and prediction fits, respectively. a) and b) show results for Dataset 1, c) and d) for Dataset 2, e) and f) for Dataset 3.

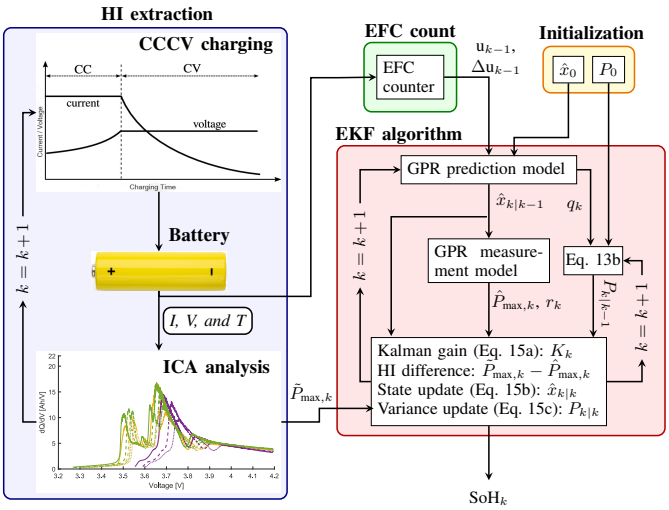

Fig. 12. Flowchart of the proposed GPR-EKF SoH estimation algorithm.

order polynomial baseline. In Dataset 2, both models achieve comparable performance, whereas in Dataset 3, GPR again surpasses the second-order polynomial model. Additionally, LSTM models are employed to represent both the prediction and measurement components and Fig. 11 shows the fitting results. In all corresponding cases, GPR models have better performance than LSTM models. These results demonstrate that GPR achieves a more sensitive and accurate fit to the characteristics of each dataset.

Battery-level open-loop performance for each model was assessed using a leave-one-battery-out validation strategy, with the results summarized in Table III. Across all three datasets, the GPR prediction model generally achieved the lowest average RMSE, calculated as the arithmetic mean of the individual battery-level RMSE values. In Dataset 1, the average RMSE values were 0.0440 for GPR, 0.0472 for the polynomial model, and 0.0564 for the LSTM model. In Dataset 2, the GPR model achieved an average RMSE of 0.0205, demonstrating performance nearly equivalent to the polynomial model (0.0204) while still outperforming the LSTM model (0.0227). In Dataset 3, the GPR model achieved an average RMSE of 0.0055, compared to 0.0095 for the polynomial model and 0.0218 for the LSTM model, demonstrating the strongest performance. For the measurement models, the GPR model generally achieved the lowest average RMSE, except in Dataset 1, where the polynomial and GPR models had similar performance. The average RMSEs for the GPR, polynomial, and LSTM models were 0.0338, 0.0336, and 0.0345 in Dataset 1; 0.0136, 0.0149, and 0.0164 in Dataset 2; and 0.0111, 0.0117, and 0.0279 in Dataset 3, respectively. Overall, the GPR models consistently delivered the lowest average errors in most cases, followed closely by the polynomial models, while the LSTM models showed comparatively weaker performance. Additionally, the GPR models offer uncertainty estimates, which is advantageous for Kalman filter applications where determining appropriate prediction and measurement variance parameters can be challenging.

The GPR predictive variance $\sigma^2(i_k)$ is interpreted as a data-driven estimate of the process noise variance. This enables a more informed prediction step within the EKF:

$$\hat{x}_{k|k-1} = \mu(i_{k-1}) \tag{13a}$$

$$P_{k|k-1} = F_{k|k-1} P_{k-1|k-1} F_{k|k-1}^{\top} + \sigma^2(i_{k-1}) \tag{13b}$$

where P is the prediction covariance. The Jacobian $F_{k|k-1}$ is numerically estimated using central finite differences:

$$F_{k|k-1} \approx \frac{\mu(i_{k-1} + \delta e_1) - \mu(i_{k-1} - \delta e_1)}{2\delta} \tag{14}$$

where $e_1 = [1, 0, 0]^T$ and δ is a small perturbation. Again, this simple finite difference can be replaced by advanced numerical differentiation methods in [36]. Similarly, a measurement GPR model is trained to relate SoH to the measurable $\mathrm{P_{max}}$. From Eq. (10), the training dataset for the model is defined as $\mathcal{D}_m = \{(\mathrm{SoH}_k, \mathrm{P_{max},}_k)\}_{k=1}^{n}$. At each calculation step, the measurement update is given by:

$$K_k = P_{k|k-1} H_k^{\top} (H_k P_{k|k-1} H_k^{\top} + r_k)^{-1} \tag{15a}$$

$$\hat{x}_{k|k} = \hat{x}_{k|k-1} + K_k \left[\tilde{z}_k - h(\hat{x}_{k|k-1})\right] \tag{15b}$$

$$P_{k|k} = (\mathbf{I} - K_k H_k) P_{k|k-1} \tag{15c}$$

where K_k is the Kalman gain, $h(\cdot)$ is the mean function of the GPR measurement model, r_k is the prediction variance from the measurement GPR model, and H_k equal to $dh(x_k)/dx_k$ is computed via finite differences, analogous to $F_{k|k-1}$. Fig. 12 summarizes the flowchart of the proposed online SoH estimation method. The proposed method eliminates the reliance on physical models and integrates EFC count and ICA-based HI measurement within an uncertainty-aware EKF framework to optimize SoH estimation. Note that the LSTM-EKF employs Jacobian calculations and model training similar to the GPR-EKF. In all methods, the prediction and measurement models are trained offline.

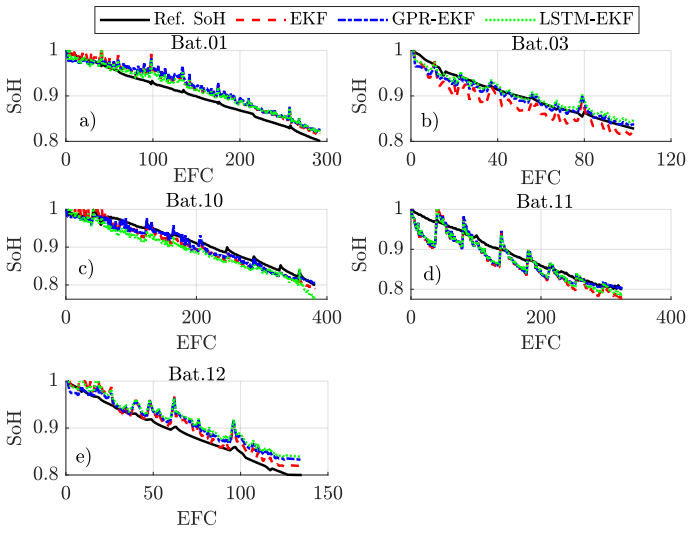

Fig. 13. (Dataset 1) SoH estimation results for batteries using standard EKF, GPR-EKF and LSTM-EKF compared to the reference SoH.

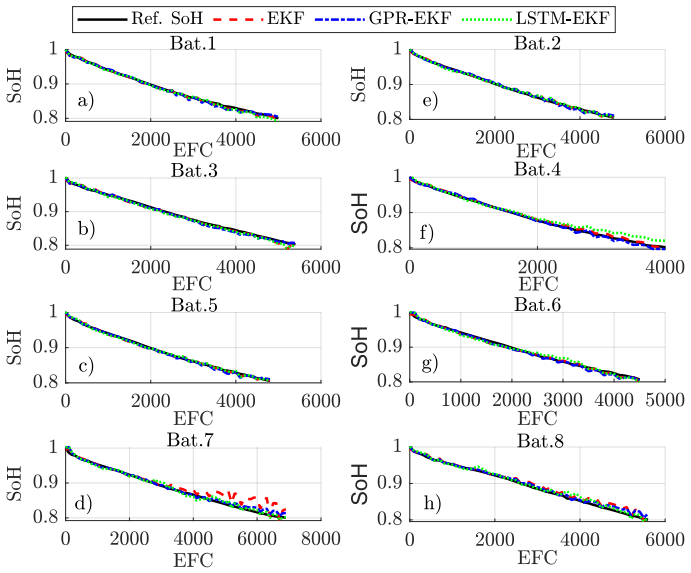

Fig. 14. (Dataset 2) SoH estimation results for batteries using standard EKF, GPR-EKF and LSTM-EKF compared to the reference SoH.

III. Experiments and Results

This section presents the performance evaluation of the proposed SoH estimation framework. It is assessed using a leave-one-battery-out validation strategy, where each battery is sequentially excluded from the training set and exclusively used for testing. Estimation accuracy is quantified through standard metrics, including RMSE and mean absolute error (MAE). Battery simulations continue until the SoH decreases to 80%, indicating the end of the useful life [43].

In standard EKF simulations, initial P, q, and r were determined by manual tuning minimizing the estimation error while maintaining stability. Each parameter was varied over a practical range, and the configuration yielding the lowest RMSE without filter divergence was selected. For Dataset 1, initial P, q, and r were set to 0.01, 0.3, and 0.2, respectively.

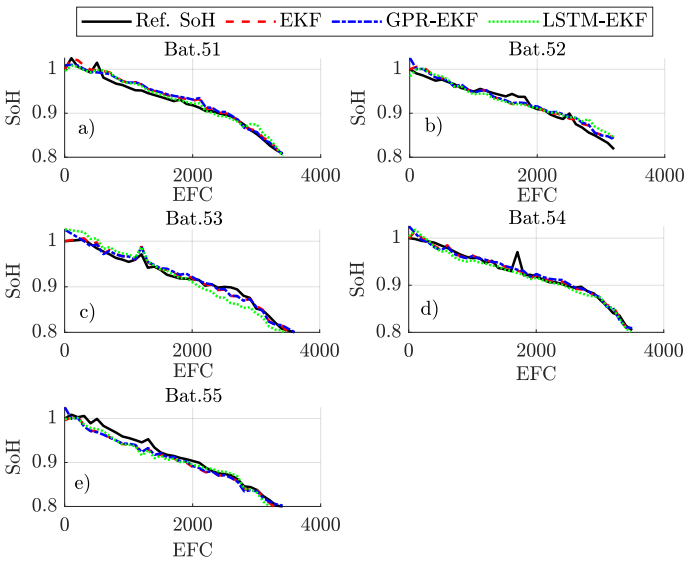

Fig. 15. (Dataset 3) SoH estimation results for batteries using standard EKF, GPR-EKF and LSTM-EKF compared to the reference SoH.

For Datasets 2 and 3, these parameters were adjusted to 0.01, 0.2, and 0.1, reflecting lower noise levels. GPR-EKF simulations maintained identical initial P for fair comparison, while q and r values were provided directly from GPR model outputs. The GPR models employed a squared-exponential kernel, with kernel scale, noise variance, and basis coefficients automatically tuned via MATLAB's Bayesian optimization [44]. The LSTM-EKF simulations were conducted with the same initial P, q, and r as the EKF for each dataset. The LSTM prediction model consisted of a sequence input layer, a 16-unit LSTM layer with last-step output, ReLU activation, dropout (0.1), a fully connected layer, and a regression layer. The LSTM measurement model followed the same structure but used an 8-unit LSTM layer without dropout. Both models were trained using the Adam optimizer for 100 epochs with a mini-batch size of 16, an initial learning rate of 1.27×10^{-3}, gradient clipping at 1, and L2 regularization of 10^{-4}. In all datasets, the reference SoH values are determined using Eq. (5).

Fig. 13 presents SoH estimation results for Dataset 1, while Table IV details battery-level SoH estimation error metrics across all datasets. In Dataset 1, the GPR-EKF method more closely follows the reference curves compared to the EKF and LSTM-EKF. The GPR-EKF achieved the lowest average errors (RMSE = 0.0188, MAE = 0.0156), outperforming the EKF (RMSE = 0.0217, MAE = 0.0186) and the LSTM-EKF (RMSE = 0.0209, MAE = 0.0183). At 0°C, the results for Battery 11 exhibited oscillations, which were attributable to reduced lithium-ion kinetics and the amplifying effect of low temperature on measurement noise and modelling errors. In detail, the RMSE of GPR-EKF was 0.0242 at 0°C, with 17.9% attributable to modelling bias and 82.1% to measurement noise. At 25°C, the RMSE decreased to 0.0122, with 37.7% arising from modelling bias and 62.3% from measurement noise. At 45°C, the RMSE was 0.0239, comprising 47.7% modelling bias and 52.3% measurement noise. During bat-

TABLE IV
COMPARISON OF SOH ESTIMATION ACCURACY ACROSS THREE DATASETS

Dataset	Battery	EKF RMSE / MAE	GPR-EKF RMSE / MAE	LSTM-EKF RMSE / MAE
Dataset 1	Bat.01	0.0198 / 0.0179	0.0213 / 0.0193	0.0171 / 0.0153
	Bat.03	0.0229 / 0.0205	0.0123 / 0.0090	0.0119 / 0.0095
	Bat.10	0.0169 / 0.0154	0.0122 / 0.0104	0.0233 / 0.0218
	Bat.11	0.0274 / 0.0229	0.0242 / 0.0186	0.0235 / 0.0189
	Bat.12	0.0214 / 0.0165	0.0239 / 0.0209	0.0289 / 0.0261
	Avg.	0.0217 / 0.0186	0.0188 / 0.0156	0.0209 / 0.0183
Dataset 2	Bat.1	0.0033 / 0.0027	0.0042 / 0.0031	0.0043 / 0.0033
	Bat.2	0.0035 / 0.0026	0.0036 / 0.0029	0.0033 / 0.0026
	Bat.3	0.0046 / 0.0036	0.0040 / 0.0034	0.0048 / 0.0038
	Bat.4	0.0044 / 0.0035	0.0036 / 0.0029	0.0103 / 0.0080
	Bat.5	0.0034 / 0.0028	0.0034 / 0.0027	0.0034 / 0.0029
	Bat.6	0.0037 / 0.0031	0.0045 / 0.0033	0.0058 / 0.0049
	Bat.7	0.0188 / 0.0130	0.0065 / 0.0046	0.0062 / 0.0050
	Bat.8	0.0091 / 0.0067	0.0062 / 0.0045	0.0065 / 0.0049
	Avg.	0.0064 / 0.0048	0.0045 / 0.0034	0.0056 / 0.0044
Dataset 3	Bat.51	0.0102 / 0.0086	0.0104 / 0.0086	0.0100 / 0.0081
	Bat.52	0.0111 / 0.0090	0.0113 / 0.0094	0.0141 / 0.0119
	Bat.53	0.0089 / 0.0072	0.0095 / 0.0076	0.0172 / 0.0148
	Bat.54	0.0091 / 0.0061	0.0088 / 0.0060	0.0108 / 0.0074
	Bat.55	0.0135 / 0.0110	0.0131 / 0.0105	0.0137 / 0.0114
	Avg.	0.0106 / 0.0084	0.0106 / 0.0084	0.0132 / 0.0107

teries' late-life stage, i.e., SoH $\in [0.80, 0.85]$, the GPR-EKF attains the lowest average RMSE and MAE among the three methods, as summarized in Table V.

In Dataset 2 shown in Fig. 14, all three approaches maintained high accuracy under stable operating conditions. However, the EKF in Battery 7 and the LSTM-EKF in Battery 4 produced relatively higher estimation errors due to significant deviations in the EFC–SoH trend compared to the other batteries. In contrast, the GPR-EKF demonstrated superior robustness to such variability. The GPR-EKF achieved the lowest average errors (RMSE = 0.0045, MAE = 0.0034), relative to the EKF (RMSE = 0.0064, MAE = 0.0048) and the LSTM-EKF (RMSE = 0.0056, MAE = 0.0044). At the late-life stage, Table V indicates that the GPR-EKF and LSTM-EKF exhibit comparable performance. Meanwhile, Fig. 14f) shows that the GPR-EKF clearly outperforms the LSTM-EKF for Battery 4 during the late-life stage.

In Dataset 3 shown in Fig. 15, the EKF and GPR-EKF achieve similar performance, and both have superior accuracy relative to the LSTM-EKF. The EKF and GPR-EKF yield nearly identical average errors (RMSE = 0.0106, MAE = 0.0084), whereas the LSTM-EKF exhibits higher error metrics (RMSE = 0.0132, MAE = 0.0107). Furthermore, Table V shows that the GPR-EKF demonstrates superior late-life stage performance compared with the other two methods.

Algorithm performances in the late-life stage were also evaluated relative to those in the full-life stage, i.e., SoH $\in [0.80, 1]$. In Dataset 2, all methods experienced some increase relative to their full-life performance. This deterioration reflects the exceptionally low errors in the full-life stage, rather than a true decline in estimation capability. Nevertheless, both the GPR-EKF and LSTM-EKF preserved high accuracy, yielding RMSE values of 0.0066 and 0.0064 and MAE values of 0.0057 and 0.0054, respectively. In Dataset 1, all algorithms improved except for a small rise in the LSTM-EKF's MAE. In Dataset 3, the EKF remained nearly unchanged. The GPR-EKF showed clear gains, while the LSTM-EKF exhibited moderate improvement. Overall, the GPR-EKF demonstrated the strongest generalization in the late-life stage, consistent with its superior performance across the full-life range.

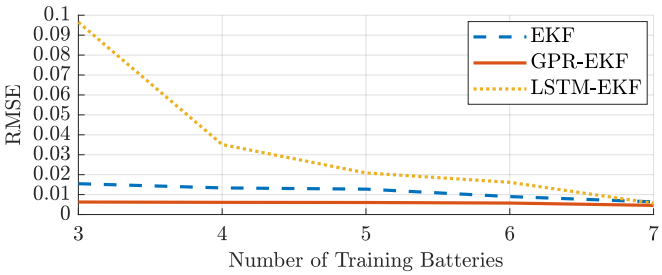

Fig. 16. Data efficiency of each algorithm on Dataset 2.

TABLE V
ESTIMATION ERRORS IN THE LATE-LIFE SOH RANGE OF 0.80–0.85.

Dataset	EKF Avg. RMSE / MAE	GPR-EKF Avg. RMSE / MAE	LSTM-EKF Avg. RMSE / MAE
Dataset 1	0.0157 / 0.0147	0.0153 / 0.0142	0.0195 / 0.0188
Dataset 2	0.0111 / 0.0098	0.0066 / 0.0057	0.0064 / 0.0054
Dataset 3	0.0104 / 0.0087	0.0073 / 0.0065	0.0116 / 0.0103

Data efficiency was evaluated on Dataset 2 by analyzing how estimation errors varied as the number of training batteries increased from three to seven. For each target battery, models were trained using a moving window of consecutive cells (for example, batteries 1–2–3, then 2–3–4, and so on), and algorithms were tested on the remaining cells. This process was repeated eight times, matching the total number of batteries in the dataset. The average error across all repetitions was then calculated to represent the error associated with each training-set size. Fig. 16 shows that the GPR-EKF maintains stable accuracy, exhibiting only a minor decline when trained on fewer batteries. The EKF similarly displays limited sensitivity to the number of training batteries. In contrast, the LSTM-EKF requires larger datasets to approach the same accuracy as the GPR-EKF.

The robustness of the GPR-EKF to intermittent measurement availability was evaluated, as shown in Fig. 17. This experiment simulated a practical BMS scenario where HI measurements are not consistently accessible. Battery 8 from Dataset 2 was selected, and an 80% probability of measurement availability was applied at each update step during the CCCV charging process. Estimation accuracy was measured using RMSE and MAE. With full HI availability, the GPR-EKF achieved 0.0062 RMSE and 0.0045 MAE. These errors increased to 0.0091 and 0.0063, respectively, when HI measurements were intermittently unavailable. The estimator maintained stability and quickly reconverged once updates resumed, indicating strong resilience to missing HI data.

The impact of uncertainty-aware modeling in the GPR-EKF was evaluated by comparing its RMSE in SoH estimation to that of a version employing the same fixed process and measurement variances as the EKF. Fig. 18 shows that including uncertainty-aware modeling reduces the RMSE for Batteries 51, 52, and 54. For Batteries 53 and 55, the performance is comparable to the fixed-variances version. These findings

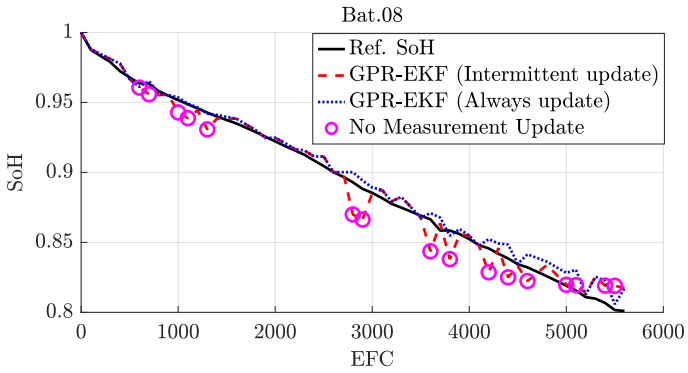

Fig. 17. SoH estimation results for Battery 8, comparing regular measurement updates (blue) with prediction-only updates applied during intervals of measurement unavailability (red).

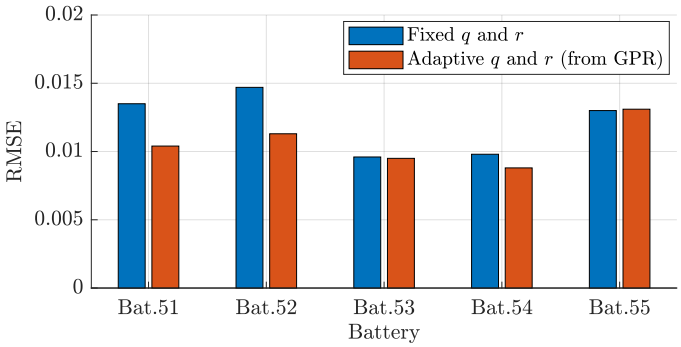

Fig. 18. Impact of uncertainty-aware modeling in the GPR-EKF on Dataset 3. The red bars represent the uncertainty-aware implementation, whereas the blue bars represent the fixed-variance implementation.

indicate that, by maintaining consistently lower or similar estimation errors across all tested batteries, uncertainty-aware modeling enhances the robustness of the GPR-EKF.

Across all methods, the computational cost remains largely unchanged because the core EKF steps are identical. On a system with an Intel® Core™ i7-1165G7 CPU at 2.80 GHz and 16 GB RAM, running MATLAB R2024b, the GPR-EKF achieved an average update time of 0.094 ms, demonstrating its lightweight computational demand. However, the GPR-EKF method leads to a higher onboard memory demand. In the EKF, only polynomial coefficients are stored, whereas the GPR-EKF retains complete trained models. For Dataset 1 (1586 samples), the prediction and measurement models occupy 4.31 MB and 4.28 MB, respectively. For Dataset 2 (520 samples), these decrease to 459 KB and 443 KB, and for Dataset 3 (389 samples), to 315 KB and 304 KB. The results confirm that memory cost scales with dataset size, with only limited influence on GPR-EKF performance, as shown in Fig. 16. Thus, the dataset size should be chosen to balance estimation accuracy and memory cost.

The results conclusively demonstrate the superior accuracy, generalization capability, and robustness of GPR-EKF. Its uncertainty-aware modeling approach enhances its robustness to irregular and unpredictable battery degradation, positioning it advantageously for practical integration into safety-critical applications such as electric vehicles and portable electronics.

IV. Conclusion and Future Work

This study introduces an adaptive EKF-based framework for SoH estimation for LIBs. The method utilizes EFC counts within the state transition model while employing the normalized peak magnitude of the IC curve as the HI within the measurement model. Polynomial models serve as initial baselines, subsequently enhanced through integration of GPR to incorporate model uncertainty and adaptability. In addition, the LSTM-EKF algorithm is implemented to provide a benchmark against the GPR-EKF.

Validation conducted with three publicly available datasets via leave-one-battery-out analysis confirms that the GPR-EKF has the lowest average RMSE on Datasets 1–2 and comparable performance to the EKF on Dataset 3. In all datasets, GPR-EKF outperforms the LSTM-EKF, reflecting better generalization and responsiveness to abrupt SoH changes. The enhanced performance of GPR-EKF is attributed to its non-parametric flexibility and probabilistic modeling framework, enabling dynamic adjustment of error covariance through explicit uncertainty quantification. Consequently, GPR-EKF exhibits improved robustness to shifts in degradation patterns and measurement noise.

Future research will investigate the impact of multi-step CC fast-charging protocols on the SoH estimation accuracy and explore sensor fusion approaches integrating multiple HI methodologies using real-world electric vehicle datasets. These developments aim to increase the applicability of the proposed method to different CC charging protocols and further capture capacity- and resistance-based degradation mechanisms, augmenting the robustness and adaptability of the proposed estimation framework.

Acknowledgments

The authors would like to express their sincere gratitude to the anonymous reviewers for their time and consideration.

Authors' Contributions

O. Kadem designed and implemented the algorithm, preprocessed the data, and conducted the simulations. J. Kim reviewed the algorithm and the results, and suggested the final test scenario. Both contributed to the writing, reviewing, and editing of the manuscript.

Data Availability

Data will be made available upon request from the authors.

References

[1] Mao, L., Wen, J., Zhao, J., & Qu, K. (2024). Online state-of-health estimation of lithium-ion batteries based on a novel equal voltage range sampling count number health indicator. IEEE Transactions on Transportation Electrification, 10(1), 2277-2292.

[2] Wei, Z., Ruan, H., Li, Y., Li, J., Zhang, C., & He, H. (2022). Multistage state of health estimation of lithium-ion battery with high tolerance to heavily partial charging. IEEE Transactions on Power Electronics, 37(6), 7432-7442.

[3] Singh, P., Chen, C., Tan, C. M., & Huang, S. C. (2019). Semi-empirical capacity fading model for SoH estimation of Li-ion batteries. Applied Sciences, 9(15), 3012.

[4] Cacciato, M., Nobile, G., Scarcella, G., & Scelba, G. (2016). Real-time model-based estimation of SOC and SOH for energy storage systems. IEEE Transactions on Power Electronics, 32(1), 794-803.

[5] Bartlett, A., Marcicki, J., Onori, S., Rizzoni, G., Yang, X. G., & Miller, T. (2015). Electrochemical model-based state of charge and capacity estimation for a composite electrode lithium-ion battery. IEEE Transactions on control systems technology, 24(2), 384-399.

[6] Kumar, P., Sundaresan, S., & Balasingam, B. (2023). Theoretical performance evaluation of battery equivalent circuit model parameter estimators. IEEE Journal of Emerging and Selected Topics in Industrial Electronics, 5(3), 1109-1119.

[7] He, L., Wang, G., Wei, Y., Yu, J., Zhao, X., & Liu, J. (2025). Multi-loop feedback proportional–integral observer for both estimation of state-of-charge and state-of-health. Energy, 329, 136456.

[8] Pan, C., Peng, Z., Yang, S., Wen, G., & Huang, T. (2024). Maximum correntropy filter-based adaptive fusion method for SOH estimation considering capacity regeneration phenomenon. IEEE Transactions on Power Electronics, 40(3), 4473–4485.

[9] Liu, K., Li, Y., Hu, X., Lucu, M., & Widanage, W. D. (2019). Gaussian process regression with automatic relevance determination kernel for calendar aging prediction of lithium-ion batteries. IEEE Transactions on Industrial Informatics, 16(6), 3767-3777.

[10] Wang, X., Hu, B., Su, X., Xu, L., & Zhu, D. (2024). State of health estimation for lithium-ion batteries using random forest and gated recurrent unit. Journal of Energy Storage, 76, 109796.

[11] X. Feng et al., "Online State-of-Health Estimation for Li-Ion Battery Using Partial Charging Segment Based on Support Vector Machine," in IEEE Transactions on Vehicular Technology, vol. 68, no. 9, pp. 8583-8592, Sept. 2019, doi: 10.1109/TVT.2019.2927120.

[12] L. Wei et al., "State of Health Estimation of Lithium-Ion Batteries Based on Relaxation Voltage Reconstruction and AM-LSTM Method," in IEEE Transactions on Transportation Electrification, vol. 11, no. 3, pp. 7261-7273, June 2025, doi: 10.1109/TTE.2025.3525557.

[13] T. Ouyang, Y. Su, C. Wang and S. Jin, "Combined Meta-Learning With CNN-LSTM Algorithms for State-of-Health Estimation of Lithium-Ion Battery," in IEEE Transactions on Power Electronics, vol. 39, no. 8, pp. 10106-10117, Aug. 2024, doi: 10.1109/TPEL.2024.3398010.

[14] Liao, W., Chen, Z., Li, P., Tan, J., Li, H., & Zhao, C. (2025). Enhanced battery health monitoring in electric vehicles: A novel hybrid HBA-HGBR model. Journal of Energy Storage, 110, 115316.

[15] Wang, F., Zhai, Z., Zhao, Z., Di, Y., & Chen, X. (2024). Physics-informed neural network for lithium-ion battery degradation stable modeling and prognosis. Nature Communications, 15(1), 4332.

[16] J. Wu, H. Su, J. Meng and M. Lin, "State of Health Estimation for Lithium-Ion Battery via Recursive Feature Elimination on Partial Charging Curves," in IEEE Journal of Emerging and Selected Topics in Power Electronics, vol. 11, no. 1, pp. 131-142, Feb. 2023, doi: 10.1109/JESTPE.2022.3177451.

[17] L. Shen, J. Li, L. Meng, L. Zhu and H. T. Shen, "Transfer Learning-Based State of Charge and State of Health Estimation for Li-Ion Batteries: A Review," in IEEE Transactions on Transportation Electrification, vol. 10, no. 1, pp. 1465-1481, March 2024, doi: 10.1109/TTE.2023.3293551.

[18] Hu, X., Jiang, J., Cao, D., & Egardt, B. (2015). Battery health prognosis for electric vehicles using sample entropy and sparse Bayesian predictive modeling. IEEE Transactions on Industrial Electronics, 63(4), 2645-2656.

[19] Kim, J., Krüger, L., & Kowal, J. (2020). On-line state-of-health estimation of Lithium-ion battery cells using frequency excitation. Journal of energy storage, 32, 101841.

[20] Fu, Y., Xu, J., Shi, M., & Mei, X. (2021). A fast impedance calculation-based battery state-of-health estimation method. IEEE Transactions on Industrial Electronics, 69(7), 7019-7028.

[21] Wang, Z., Zeng, S., Guo, J., & Qin, T. (2019). State of health estimation of lithium-ion batteries based on the constant voltage charging curve. Energy, 167, 661-669.

[22] Guo, Z., Qiu, X., Hou, G., Liaw, B. Y., & Zhang, C. (2014). State of health estimation for lithium ion batteries based on charging curves. Journal of Power Sources, 249, 457-462.

[23] Schaltz, E., Stroe, D. I., Nørregaard, K., Ingvardsen, L. S., & Christensen, A. (2021). Incremental capacity analysis applied on electric vehicles for battery state-of-health estimation. IEEE Transactions on Industry Applications, 57(2), 1810-1817.

[24] Honarvar, F., & Varvani-Farahani, A. (2020). A review of ultrasonic testing applications in additive manufacturing: Defect evaluation, material characterization, and process control. Ultrasonics, 108, 106227.

[25] Yue, J., Xia, X., Zhang, Y., & Xia, T. (2023). A State-of-Health Estimation and Prediction Algorithm for Lithium-Ion Battery of Energy Storage Power Station Based on Information Entropy of Characteristic Data. Journal of Electrical Engineering & Technology, 18(3), 1757-1768.

[26] Wu, B., Yufit, V., Merla, Y., Martinez-Botas, R. F., Brandon, N. P., & Offer, G. J. (2015). Differential thermal voltammetry for tracking of degradation in lithium-ion batteries. Journal of power sources, 273, 495-501.

[27] L. Chen et al., "Remaining Useful Life Prediction of Battery Using a Novel Indicator and Framework With Fractional Grey Model and Unscented Particle Filter," in IEEE Transactions on Power Electronics, vol. 35, no. 6, pp. 5850-5859, June 2020, doi: 10.1109/TPEL.2019.2952620.

[28] Dubarry, M., Svoboda, V., Hwu, R., & Liaw, B. Y. (2006). Incremental capacity analysis and close-to-equilibrium OCV measurements to quantify capacity fade in commercial rechargeable lithium batteries. Electrochemical and solid-state letters, 9(10), A454.

[29] J. Wang et al., "Multiple Indicators-Based Health Diagnostics and Prognostics for Energy Storage Technologies Using Fuzzy Comprehensive Evaluation and Improved Multivariate Grey Model," in IEEE Transactions on Power Electronics, vol. 36, no. 11, pp. 12309-12320, Nov. 2021, doi: 10.1109/TPEL.2021.3075517.

[30] Stroe, D. I., & Schaltz, E. (2018, September). SOH estimation of LMO/NMC-based electric vehicle lithium-ion batteries using the incremental capacity analysis technique. In 2018 IEEE energy conversion congress and exposition (ECCE) (pp. 2720-2725). IEEE.

[31] Wei, Z., Li, Y., Sun, X., Liu, W., Liu, C., & Lu, H. (2025). SOH estimation of lithium-ion batteries based on multi-feature extraction and improved DLEM. Journal of Energy Storage, 120, 116460.

[32] Li, Y., Abdel-Monem, M., Gopalakrishnan, R., Berecibar, M., Nanini-Maury, E., Omar, N. & Van Mierlo, J. (2018). A quick on-line state of health estimation method for Li-ion battery with incremental capacity curves processed by Gaussian filter. Journal of Power Sources, 373, 40-53.

[33] Li, X., Yuan, C., & Wang, Z. (2020). State of health estimation for Li-ion battery via partial incremental capacity analysis based on support vector regression. Energy, 203, 117852.

[34] Anseán, D., García, V. M., González, M., Blanco-Viejo, C., Viera, J. C., Pulido, Y. F., & Sánchez, L. (2019). Lithium-ion battery degradation indicators via incremental capacity analysis. IEEE Transactions on Industry Applications, 55(3), 2992-3002.

[35] Taylor, J., Barai, A., Ashwin, T. R., Guo, Y., Amor-Segan, M., & Marco, J. (2019). An insight into the errors and uncertainty of the lithium-ion battery characterisation experiments. Journal of Energy Storage, 24, 100761.

[36] Van Breugel, Floris, J. Nathan Kutz, and Bingni W. Brunton. (2020). Numerical differentiation of noisy data: A unifying multi-objective optimization framework. IEEE Access, vol. 8, 196865-196877.

[37] P. Mohtat, S. Lee, J.B. Siegel, A.G. Stefanopoulou, Reversible and irreversible expansion of lithium-ion batteries under a wide range of stress factors, J.Electrochem. Soc. 168 (10) (2021) 100520.

[38] Birkl, C. (2017). Oxford Battery Degradation Dataset 1. University of Oxford.

[39] B. Nowacki, J. Ramamurthy, A. Thelen, C. Tischer, C. L. Pint, and C. Hu, "Rapid estimation of lithium-ion battery capacity and resistances from short duration current pulses," Journal of Power Sources, vol. 628, p. 235813, Feb. 2025, doi: 10.1016/j.jpowsour.2024.235813.

[40] M. Yu, Y. Zhu, X. Gu, Q. Zhang and Y. Shang, "Incremental Expansion Analysis and State-of-Health Estimation for Lithium-Ion Batteries," in IEEE Transactions on Industrial Electronics, Early Access (2025), doi: 10.1109/TIE.2025.3587113.

[41] Guan, T., Sun, S., Gao, Y., Du, C., Zuo, P., Cui, Y., & Yin, G. (2016). The effect of elevated temperature on the accelerated aging of LiCoO2/mesocarbon microbeads batteries. Applied Energy, 177, 1-10.

[42] Rasmussen, C. E. (2003). Gaussian processes in machine learning. In Summer school on machine learning (pp. 63-71). Berlin, Heidelberg: Springer Berlin Heidelberg.

[43] Lin, C., Tang, A., & Wang, W. (2015). A review of SOH estimation methods in Lithium-ion batteries for electric vehicle applications. Energy Procedia, 75, 1920-1925.

[44] MathWorks, *fitrgp: Fit Gaussian process regression (GPR) model*, https://www.mathworks.com/help/stats/fitrgp.html, accessed September 30, 2025.